Dual Luminescent Mn(II)-Doped Cu-In-Zn-S Quantum Dots as Temperature Sensors in Water

*Caterina Bellatreccia, Zakaria Ziani, Angelica Germinario, Stijn Engelaar, Filippo Piero Battaglia, Alessandro Gradone, Marco Villa, and Paola Ceroni**

$CuInS_2$ quantum dots have emerged in the last years as non-toxic alternative to traditional Pb and Cd based quantum dots, especially for biological applications. In this work, the hydrothermal synthesis of alloyed Cu-In-Zn-S quantum dots (CIZS) doped with manganese(II) is explored, with different metal ratios (Mn-CIZSy). The doped quantum dots show the sensitized emission of Mn^{2+} (approximately ms lifetime), together with the emission of the CIZS structure (approximately μs lifetime). The relative contribution of Mn^{2+} emission is highly dependent on the composition of the CIZS hosting structure (In:Cu ratio). In addition to that, it is shown that Mn^{2+} sensitization requires a threshold energy, which suggests the involvement of an intermediate state in the sensitization mechanism. The long-lived emission intensity decay of Mn^{2+} shows a stable and reversible temperature response in physiological conditions (25–45 °C, pH = 7.4). Mn-CIZSy quantum dots are thus interesting candidates as biological luminescent temperature probe thanks to their easy synthesis, high colloidal stability, insensitivity to dioxygen quenching and quantitative time-gated detection.

1. Introduction

In the last decades, quantum dots (QDs) have attracted increasing interest in the scientific community for their outstanding optical properties.[1–3] Their tunability and stability proved to be particularly suitable to the field of optical sensors.[4–6] In this

C. Bellatreccia, Z. Ziani[+], A. Germinario, S. Engelaar, F. P. Battaglia, M. Villa, P. Ceroni
Dipartimento di Chimica "Giacomo Ciamician"
Alma Mater Studiorum – Università di Bologna
Via Selmi 2, Bologna 40126, Italy
E-mail: paola.ceroni@unibo.it
A. Gradone
Istituto per la Microelettronica ed i Microsistemi (IMM) - CNR Sede di Bologna
via Gobetti 101, Bologna 40129, Italy

The ORCID identification number(s) for the author(s) of this article can be found under https://doi.org/10.1002/smll.202404425

[+]Present address: CNRS, Laboratoire de Chimie de Coordination (LCC), 205 Rte de Narbonne, Toulouse 31400, France

context, temperature is one of the most important parameters that regulates biological processes and affects material properties in diverse technological applications. Among others, luminescence thermometry takes advantage of temperature-related changes in the photoluminescence properties (lifetime, emission intensity and/or peak position) to measure temperature in the local environment of the luminescent probe.[7] It has received much attention because of its fast response, ease of implementation, high spatial resolution, and possibility of remote handling.[7,8] Quantum dots have already been proposed as suitable luminescent temperature sensors.[6,9] However, conventional IV-VI, II-VI, and III-V QDs have found limited use in the biological field, due to the intrinsic toxicity of heavy metals such as Pb and Cd. In this context, I-III-VI QDs such as $CuInS_2$ have been proposed as non-toxic and green alternatives to conventional quantum dots.[10–13] $CuInS_2$ (CIS) quantum dots are ternary direct-bandgap semiconducting nanocrystals, which ensures great tunability and high absorption coefficients in the visible spectral range.[14] In addition to that, they are generally considered non-toxic when passivated with ZnS shell, which also improves their photoluminescence quantum yield (PLQY).[15,16] Their ternary nature offers easier modulation of their photophysical properties by changing the composition of the nanocrystal, particularly acting on the In:Cu ratio.[17,18] Their crystal structure is tolerant to the insertion of doping agents and, among others, manganese(II) has proven to be an excellent dopant, displaying a sensitized long-lived luminescence in the order of milliseconds. It is worth noting that, while such long-lived emission is already well documented in quantum dots, it is usually reported for systems synthesized with solvothermal or hot-injection techniques, which make use of organic solvent and high temperatures.[19–23] It is instead rarely studied on water-based quantum dots synthesized at low temperature, and the few examples present in the literature focus on their application in photoelectrochemical cells and light emitting diodes.[24,25]

The long-lived emission of Mn^{2+} combined with the biocompatibility of CIS/ZnS quantum dots are a perfect match for their use in the field of luminescence thermometry. Because of their high molar absorption coefficient, the hosting quantum dots can function as light-harvesting antennae,[26,27] transferring excitation energy to the guest Mn^{2+} ion, which displays very low

**ADVANCED
SCIENCE NEWS**

www.advancedsciencenews.com

NANO · MICRO

small

www.small-journal.com

$MnSO_4$
$+ CuCl_2$
$+ InCl_3$

1) Na_2S, *L*-GSH, sodium citrate
2) $Zn(OAc)_2$, Thiourea, *L*-GSH
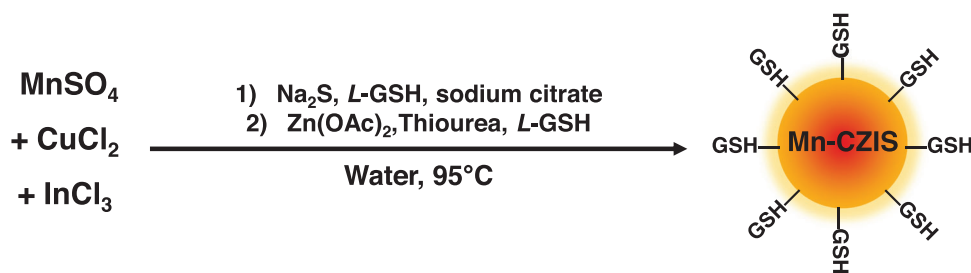
Water, 95°C

→ Mn-CZIS (with GSH ligands)

Figure 1. Schematic procedure for the synthesis of Mn-CIZSγ samples, where *L*-GSH stands for *L*-glutathione. In:Cu feeding ratio is varied between 2 and 30.

molar absorption coefficient. In addition to that, the quantum dots enhance the Mn^{2+} PLQY by protecting it from external quenchers, such as dioxygen. Indeed, even highly concentrated air-equilibrated aqueous solutions of Mn^{2+} do not display any detectable luminescence. In other words, the incorporation of Mn^{2+} in CIZS nanocrystals enhances the brightness of the probe, i.e., the product of the molar absorption coefficient at the excitation wavelength and the PLQY of the emitting system. At the same time, the long-lived phosphorescence of Mn^{2+} allows time-gated measurements, convenient to the use of these probes in real samples where short-lived autofluorescence and scattered light poses serious issues of detectability.[28,29]

In the present work, we report a low-temperature hydrothermal synthesis of Mn-doped Cu-In-Zn-S QDs (CIZS-QDs). We analyzed the photophysical properties of the doped quantum dots, investigating the effect of different In:Cu ratios. Furthermore, given the water solubility of our system, we tested the applicability of Mn-doped CIZS-QDs as luminescent temperature sensors under physiological conditions (25–45 °C, pH 7.4).

2. Preparation and Structural Characterization of Quantum Dots

The quantum dots were synthesized according to a modified hydrothermal procedure (**Figure 1**).[18] The experimental conditions were adjusted to ensure a good colloidal stability of the nanocrystals in water and to maximize their brightness: for example, the ratio between *L*-glutathione and sodium citrate was set to 1:1.33. In the second synthetic step, Zn^{2+} ions diffuse within the nanocrystal core forming quaternary CIZS quantum dots, as already reported for similar systems.[30,31] CIZS-QDs with In:Cu ratio from 2:1 to 37:1 were prepared, as well as a family of CIZS-QDs with constant feeding In:Cu ratio 8:1 and increasing feeding amount of Mn^{2+} (from 5% to 50% with respect to indium).

The actual content of metal ions in the nanocrystals was assessed by atomic emission spectroscopy. Prior to digestion with concentrated nitric acid, samples were purified from metal precursors by precipitation in acidic conditions (pH = 3) and centrifugation. Note that this treatment is different from standard purification procedures, which precipitate quantum dots upon addition of organic solvents, and our approach resulted in a better purification (see Supporting Information for a comparison of the two methods). Elemental analysis indicates that the In:Cu ratio is higher with respect to the feeding ratio (Table S1, Supporting Information), suggesting that indium is somewhat more reactive than copper under our synthetic conditions. The Zn:In ratio is

around 2 in all the analyzed batches, therefore an increase in the In:Cu ratio also results in an increase of the Zn:Cu ratio. In addition, elemental analysis reveals that only a small fraction of the Mn^{2+} ions is incorporated in the nanocrystals, leading to doping levels in the range 0.3–0.7% with respect to indium (Table S1, Supporting Information). For the sake of clarity, hereafter CIZS-QDs are named CIZSγ and Mn-CIZSγ, where γ refers to the actual In:Cu ratio.

The X-ray diffraction (XRD) patterns of all samples show peaks at 28.2°, 46.8° and 55.6°, characteristic of zinc-blende CIZS structure[32–34] (Figure S1, Supporting Information): change of In:Cu ratio and Mn^{2+} doping does not alter the crystal phase of quantum dots. This has already been extensively demonstrated for Cu-deficient CIS quantum dots, and it is often explained by the fact that Cu^+ and In^{3+} occupy the same crystallographic locations in the zinc-blende phase, enabling variable stoichiometry within the same crystal structure.[17,35,36] In addition to that, ZnS, $CuInS_2$ and In_2S_3 show structural similarities that allow a change of the metal ratio without modification of the crystalline phase.[37] The dimension of the crystallites calculated through Sherrer formula is comprised within 1.6 and 1.8 nm (See Supporting Information for details).

Dynamic light scattering measurements indicate that the hydrodynamic radius of the nanocrystals in distilled water is around 5.0 nm, irrespective of the In:Cu ratio or the presence of Mn^{2+} (Figures S2 and S3, Supporting Information). This finding agrees with the crystallite size obtained from XRD patterns, considering the steric hindrance of the ligands and the water molecules present in the hydrodynamic sphere.

High resolution transmission electron microscopy (HR-TEM) analysis in Figure S4 (Supporting Information) allows a deep understanding of the differences between the doped and undoped samples. The general morphology of CIZS11 and Mn-CIZS10 shows the presence of aggregates of small nanoparticles enclosed in an amorphous matrix. The crystalline character of the nanoparticle indicates a general d-spacings of 0.32 nm, that perfectly matches with the results obtained in powder XRD. The amorphous phase that holds the nanoparticles together probably belongs to the organic ligands attached to the crystalline core.

Scanning electron microscopy (STEM) micrographs are shown in Figure S4 (Supporting Information) for the sample with (Figure S4C, Supporting Information) and without (Figure S4D, Supporting Information) Mn^{2+} doping. The STEM technique allows aggregates to be observed with a higher spatial resolution due to higher contrast. In this case, unlike the conventional TEM technique, the contrast obtained from an image is caused by the
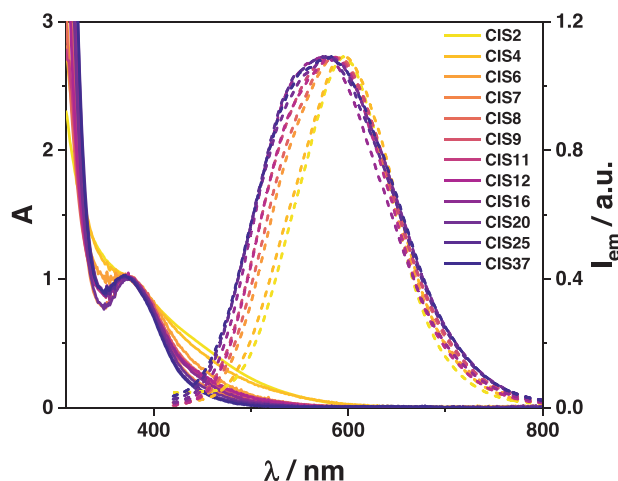
**ADVANCED
SCIENCE NEWS**

www.advancedsciencenews.com

NANO · MICRO

small

www.small-journal.com

Figure 2. Absorption (solid line) and normalized emission spectra (dashed line) of CIZSγ samples in air-equilibrated aqueous solution at room temperature. λ_{ex} = 350 nm.

ratio between atomic weight and density of the observed material, namely Z-Contrast. The results of these analyses confirm what has already been observed with HR-TEM regarding the presence of nanometric particles held together by an amorphous matrix. In addition, an average size of nanoparticles below 2 nm can be defined, in line with the results of XRD and DLS analysis. Energy dispersive X-ray spectroscopy (EDS) analysis confirmed the presence of Mn in the doped sample, while the undoped sample does not display its diagnostic peaks.

It is worth noting that the samples prepared are stable in bidistilled water for several months, and that the photophysical properties are retained even after redissolution of dried samples.

3. Photophysical Properties

The absorption spectra of CIZSγ samples (**Figure 2**) display the band-edge transition at 375 nm for all the investigated samples: a change in the In:Cu ratio has no significant effect on the bandgap energy,[38] as well as Mn^{2+} doping (Figure S6, Supporting Information). This band-edge transition becomes gradually more defined as the copper content of the nanocrystal is lowered (In:Cu ratio from 2 to 37) and concomitantly the tail extending in the visible spectral region is diminished. For example, the absorption of CIS2 and Mn-CIS2 extends up to 650 nm, while the absorption of CIS37 and Mn-CIS35 is limited to λ < 500 nm (Figure 2). This trend is related to the decrease of Cu-defects, which sharpens the band-edge transition by eliminating the sub-bandgap tail.[17,35,39] It is worth noting that no feature ascribable to Mn^{2+} ions is observed in the absorption spectra of Mn-CIZSγ samples: this result is expected given the low amount of Mn^{2+} (0.3–0.7%) and the extremely low molar absorption coefficient of the spin-forbidden electronic transitions (Figure S17, Supporting Information).[40]

To elucidate the role of Zn(II) ions on the photophysical properties, samples without the Zn(II) acetate addition (step 2 in Figure 1), hereafter named as CISγ, were prepared. The excitonic peak of CIZSγ is blue-shifted of 400 meV with respect to CISγ (Figure S7, Supporting Information), demonstrating that

the spectra of CIZSγ are not a mere overlap of two independent components, namely CIS core and ZnS shell. This indicates that Zn^{2+} ions diffuse within the core of the nanoparticles, as previously reported,[30,31] producing alloyed CIZS quantum dots, rather than core–shell structures. Interestingly, all the analyzed samples show an additional absorption shoulder at high energies (4.5 eV), which becomes more and more evident in Cu-deficient samples. The same band is observed in the control sample synthesized as reported in Figure 1, but in the absence of copper (IZS, Figure S8, Supporting Information). Therefore, the absorption feature at 4.5 eV is assigned to the alloyed ZnS-In_2S_3 structure, which is predominant in highly Cu-deficient samples. On the other hand, IZS does not display the shoulder located at 375 nm, which is characteristic of CIZS and Mn-CIZS samples, confirming that it can be ascribed to copper-related states.

The emission spectra of CIZSγ samples display a maximum around 580–600 nm: a slight broadening of the band on the high-energy side is observed upon increasing the In:Cu ratio (Figure 2). The PLQY increases with higher In:Cu ratios, reaching a plateau of 7% when In:Cu ratio is around 5 (Table S3, Supporting Information). The insertion of Mn^{2+} brings about a change of the shape of the emission band and the appearance of a new red-shifted component (**Figure 3A**), compatible with Mn^{2+} emission profile, as previously reported in literature for Mn-doped quantum dots.[41–43]

The decay of the emission intensities of all the CIZSγ samples is biexponential with an average lifetime in the order of 0.1–1 µs, which rises with increasing In:Cu ratio, in agreement with the increase in PLQY (Table S3, Supporting Information). Mn-CIZSγ samples show an additional component with longer lifetime (τ = 1.9 ms), independent from the In:Cu ratio of the nanocrystal (Figures S10 and S11, Supporting Information). We attribute this long-lived emission to the spin-forbidden $^4T_1 \rightarrow {}^6A_1$ electronic transition of Mn^{2+} ions.[19,23] Mn-doped samples showed both the emission related to the CIZS lattice ($\tau \approx 10^{-7} - 10^{-6}$ s, hereafter referred to as CIZS emission) and the one related to Mn^{2+} centers ($\tau \approx 10^{-3}$ s, hereafter referred to as Mn^{2+} emission). Considering the significant difference in the timescale of the two emission decays, the two emission components are easily discriminated by time-gated emission measurements. The emission related to CIZS in Mn-CIZSγ samples is superimposable with the corresponding CIZSγ samples, indicating that the energy of the emissive states of CIZS is not affected by the dopant (Figure 3B). All Mn-doped samples show the long-lived and sharp Mn^{2+} emission band peaked around 600–630 nm (Figure 3B). The position of the peak indicates that the coordination of Mn^{2+} in the crystal lattice is octahedral, as already reported for $CuInS_2$ quantum dots synthesized in organic solvents.[23,32] In fact, it is well known that octahedrally coordinated Mn^{2+} centers present red emission (around 600–650 nm), contrarily to tetrahedrally coordinated Mn^{2+} which show green emission (around 530–570 nm).[44] Furthermore, the intensity of Mn^{2+} emission is strongly dependent on the In:Cu ratio: the contribution of Mn^{2+} to the overall emission of Mn-CIZSγ samples, estimated by convolution of time-gated emission spectra (see experimental section for details), increases upon decreasing copper content in Mn-CIZSγ samples (Figure 3B, inset). In addition to that, increased Mn:In ratios in the nanocrystal leads to higher Mn^{2+} contribution to the overall emission (Figure S15, Supporting Information).

ADVANCED
SCIENCE NEWS
www.advancedsciencenews.com

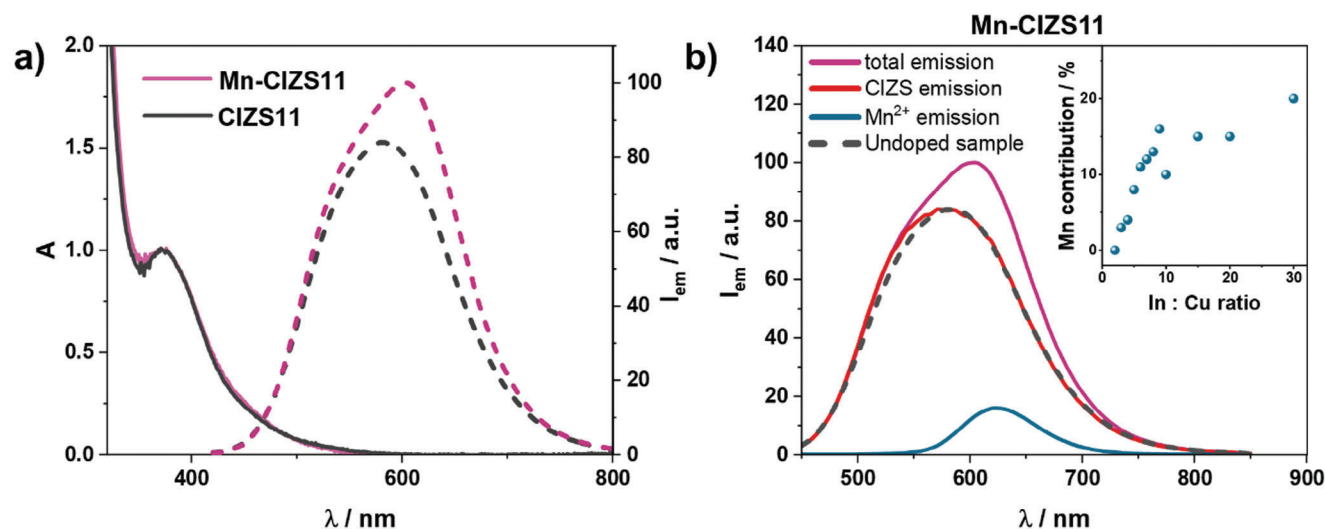NANO · MICRO
small
www.small-journal.com

Figure 3. a) Absorption (solid line) and normalized emission spectra (dotted line) of CIZS11 and Mn-CIZS11 in air-equilibrated aqueous solution. b) Emission spectra of Mn-CIZS11 with different time gates: 0–5 ms (violet), 0–0.02 ms (red, CIS emission component) and 0.2–5 ms (blue, Mn^{2+} emission component). Emission spectrum of CIZS11 is reported in black, dashed line for reference. $\lambda_{exc} = 350$ nm. The intensities are scaled on the relative contribution of Mn^{2+} and CIZS emissions. Inset: Calculated Mn^{2+} contribution corresponding to different In:Cu ratios.

Time-gated excitation spectra of Mn-CIZSγ samples were recorded in order to discriminate the short-lived CIZS emission by the long-lived Mn^{2+} emission in the excitation spectra (see Mn-CIZS11 in **Figure 4A**, while other representative ratios are analyzed in Figure S16, Supporting Information). The excitation spectrum of CIZS emission is in good agreement with the corresponding absorption spectrum of the investigated sample. The excitation spectrum of Mn^{2+} emission shows the characteristic peak of CIZS band-edge transition at 375 nm, and no additional features ascribable to Mn^{2+} absorption (see pink line in Figure 4A for the absorption spectrum of Mn^{2+} in water). This result demonstrates that Mn^{2+} emission is sensitized by the CIZS

lattice and is not arising by direct absorption of light of the Mn^{2+} centers.

It is worth noting that the Mn^{2+} excitation spectrum deviates from the Mn-CIZS11 absorption spectrum in the low energy region (Figure 4A), where the tail associated to copper-based intra-bandgap states is missing. The onset of the excitation spectrum is at 2.5 eV, irrespective of the In:Cu ratio. This finding demonstrates that excitation of the copper-based intra-bandgap states (below 2.5 eV) does not sensitize the Mn^{2+} emission. This becomes even more evident by the inspection of Figure 4B, where the contribution of Mn^{2+} to the overall emission of Mn-CIZS11 is plotted as a function of the excitation energy. The Mn^{2+}
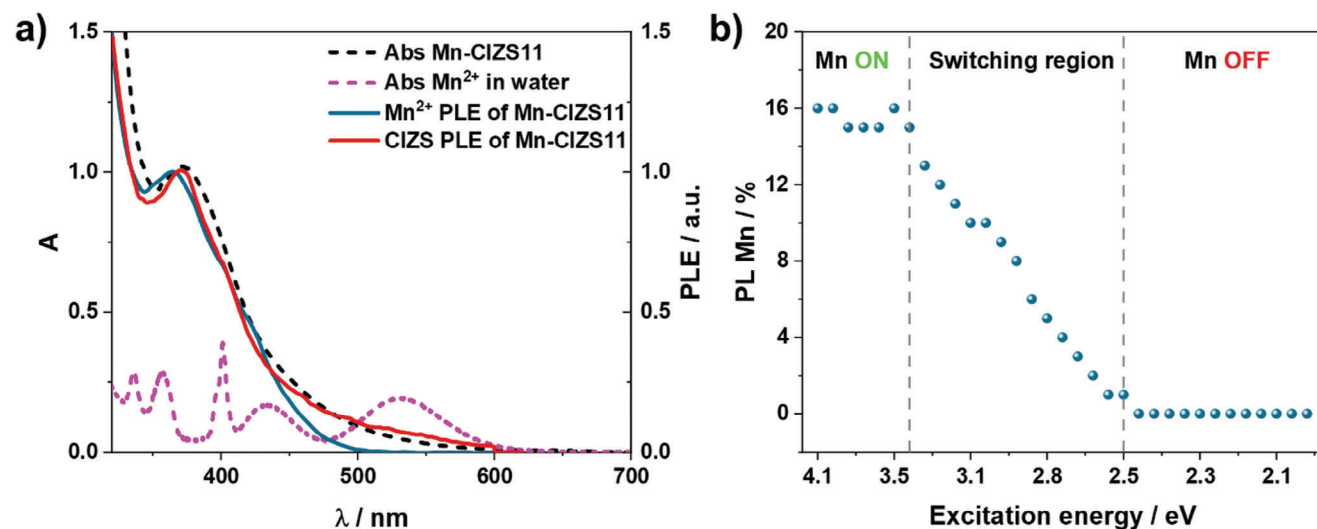

Figure 4. a) Excitation spectra ($\lambda_{em} = 640$ nm) of Mn-CIZS11 recorded with time gate 0.2–5 ms (blue line), and 0–5 ms (red line) gate. Absorption spectra of Mn-CIZS11 and MnSO$_4$ (2.5 M) in water are shown in black and pink lines, respectively. b) Calculated Mn^{2+} contribution in Mn-CIZS11 emission at different excitation wavelengths.

ADVANCED
SCIENCE NEWS
www.advancedsciencenews.com

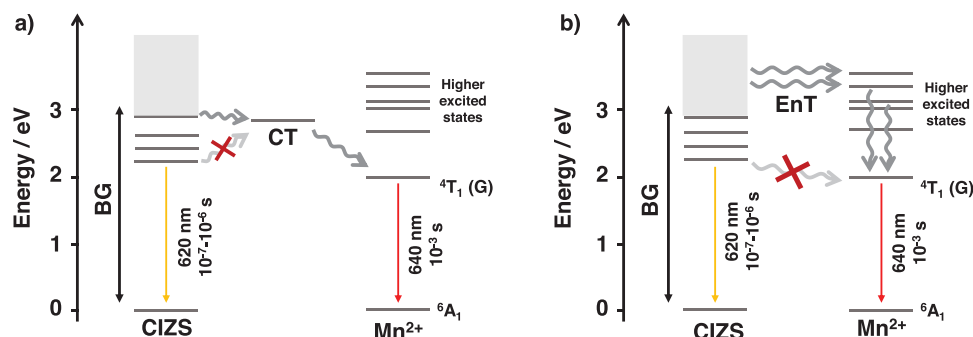NANO · MICRO

small
www.small-journal.com

Figure 5. Schematic depiction of the proposed mechanism based on the population of a) a transient charge transfer state (CT) or b) of higher energy levels of Mn^{2+}. The energies of the excited states of Mn^{2+} and CIZS are derived from absorption and emission spectra of Mn-CIZS11 and $MnSO_4$ in water (see Supporting Information).

contribution shows the following behavior: i) constant when E_{exc} is higher than 3.5 eV (Mn-ON region), ii) linear decrease upon excitation between 2.5 and 3.5 eV (switching region), iii) zero when E_{exc} is below 2.5 eV (Mn-OFF region). In addition to that, Mn^{2+} contribution to the total emission is higher in Cu-deficient quantum dots, where sub-bandgap states are less prominent.

These experimental results demonstrate that excitation at energy lower than 2.5 eV does not populate the emissive $^4T_1$ state of Mn^{2+}, although its energetic location (2 eV) makes the process energetically favorable, but it results in the CIZS emission originated by sub-bandgap states. On the other hand, upon excitation at energy higher than 2.5 eV, two competing deactivation channels are possible: i) population of CIZS emissive states or ii) population of the excited state of Mn^{2+} centers. This finding is also confirmed by the fact that the copper content in the Mn-CIZSγ samples affects the contribution of Mn^{2+} to the emission, while it does not alter its emission lifetime (Figure S11, Supporting Information). In addition to that, CIZS emission is not affected by the presence of Mn^{2+}, as highlighted in Figure 3. Therefore, the population of CIZS emissive states and Mn^{2+} excited state are competing but non-communicating processes.

The mechanism of energy transfer from quantum dots to Mn^{2+} centers has long been debated.[42,45,46] Recently, Gahlot et al. have reported spectroscopic evidence of a transient charge-transfer state involving the generation of Mn^{3+} that recombines to populate the luminescent $^4T_1$ excited state of Mn^{2+} in Mn-doped $Cd_xZn_{1-x}S$ quantum dots (**Figure 5A**).[47] The minimum energy needed to obtain Mn^{2+} sensitization is therefore the energy needed for the population of the charge transfer state, which is claimed to be approximately 2.5 eV, well in agreement with our finding.

An alternative hypothesis is that the luminescent $^4T_1$ excited state of Mn^{2+} cannot be populated upon excitation below 2.5 eV because it is not well aligned with the intra-bandgap states in the nanocrystal. Conversely, Mn^{2+} higher excited states are located within the CIZS's continuous band of high-energy states (Figure 5B), which facilitates the energy transfer to these higher states, which subsequently deactivate to Mn^{2+} ($^4T_1$), triggering its characteristic emission.

A similar phenomenon is reported for lanthanide complexes: sensitization of their emission upon excitation of the ligand is efficient only when the sensitizing excited state of the ligand is close in energy to that of the luminescent excited state of the lanthanide ion.[48] Furthermore, also for the sensitization of lanthanide metal ion, the involvement of intermediate charge-transfer state has been demonstrated.[49]

4. Sensing Properties of Mn-Doped QDs

As previously mentioned, Mn-CIZSγ are water-soluble, photostable and biocompatible, which lead us to consider them for applications in the optical sensing. To this purpose, the photoluminescence temperature dependency of Mn-CIZS11 has been studied for luminescence thermometry applications.

Mn-CIZS11 shows a linear decrease in luminescence intensity with increasing temperature, as commonly observed for luminescent materials (**Figure 6A**).[50,51] Contrarily to common fluorophores, the emission peak slightly blue-shifts (around 0.6 meV K^{-1}) upon increasing temperature. This is ascribed to decreasing contribution of Mn^{2+} emission at higher temperatures, which favors CIZS emission, located at higher energy. Indeed, heating from 10 °C to 80 °C causes the Mn^{2+} contribution for Mn-CIZS11 to drop from 16% to 11% (Figure 6B).

Emission intensity is not an ideal variable for temperature sensing applications: in fact, it can be difficult to quantify the number of absorbed and emitted photons by the probe in highly scattering media.[5] Therefore, the lifetime dependence on temperature was evaluated for Mn-CIZS11. Both CIZS and Mn^{2+} emission in Mn-CIZS11 show decreasing lifetime with temperature in the range 10–80 °C (**Figure 7**). The average photoluminescence lifetime of CIZS and Mn^{2+} decreases linearly by 9 ns K^{-1} and 13 µs K^{-1}, respectively. These values correspond to 0.9% K^{-1} and 0.7% K^{-1} relative to CIZS and Mn^{2+} emission lifetime at room temperature. This effect is ascribed to an increase of the rate of nonradiative transitions.[50–52]

Looking at biological sensing applications, we analyzed the dependence of the lifetime over a smaller temperature range (25–45 °C) in physiological phosphate buffer (PBS, pH = 7.4). Mn^{2+} emission was selected for this study, because of its favorable characteristic to the purpose. Indeed, the long-lived Mn^{2+} emission allows gated emission measurements, which suppress scattered excitation light and short-lived autofluorescence of the sample.[28] In addition to that, Mn^{2+} emission can be fitted via a monoexponential decay. This aspect greatly improves reproducibility and consistency of results, as highlighted by the
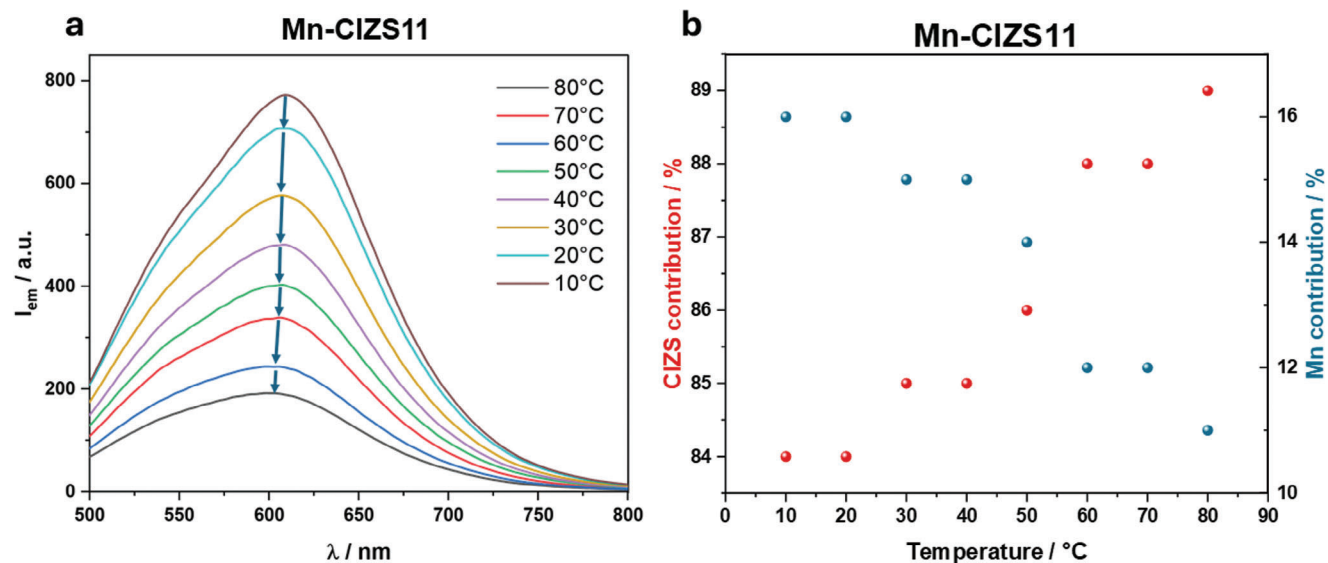
**ADVANCED
SCIENCE NEWS**
www.advancedsciencenews.com

**NANO · MICRO
small**
www.small-journal.com

Figure 6. a) Emission spectra of Mn-CIZS11 at different temperatures and b) corresponding CIZS and Mn^{2+} emission contributions. $\lambda_{exc} = 350$ nm.

significantly lower error on these measurements and the better reproducibility over cycles (Figures 7 and S22, Supporting Information). Mn^{2+} emission of Mn-CIZS11 in PBS shows a linear decrease in the range 25–45 °C, with slope 15 μs K^{-1}, corresponding to 0.8% K^{-1} (Figure 7, inset). The thermal dependence of luminescence lifetime is completely reversible (Figures S21 and S22, Supporting Information) and quantum dots are stable in PBS for several weeks (Figure S20, Supporting Information). In addition to that, Mn^{2+} lifetime of Mn-CIZS11 has proven to be independent on oxygen concentration (Figure S18, Supporting Information) and stable within the physiological pH window (Figure S19, Supporting Information). The photophysical properties of Mn-CIZS11 remain unchanged in PBS at 37.5 °C for 72 h (Figure S25, Supporting Information) and proved to be independent upon mixing Mn-CIZS11 with selected amino

acids and common anions (Figures S23 and S24, Supporting Information). It is important to note that, while ternary quantum dots have already been proposed as temperature sensors in previous reports (Table S4, Supporting Information), their thermoresponsive properties have mostly been studied in solid-state matrices[13,53] or organic solvents.[54] The few examples reporting water-soluble thermoresponding quantum dots analyze their properties in bidistilled water,[55,56] which is not mimicking the complex ionic environment in real samples. On the other hand, our system has proven to be stable and working in the physiological temperature and pH conditions (PBS buffer). In addition to that, the comparison with previous examples (Table S4, Supporting Information) shows that our system provides similar or superior sensitivity when compared to similar non-toxic systems. These characteristics make Mn-CIZSγ interesting candidates for optical thermometry applications.
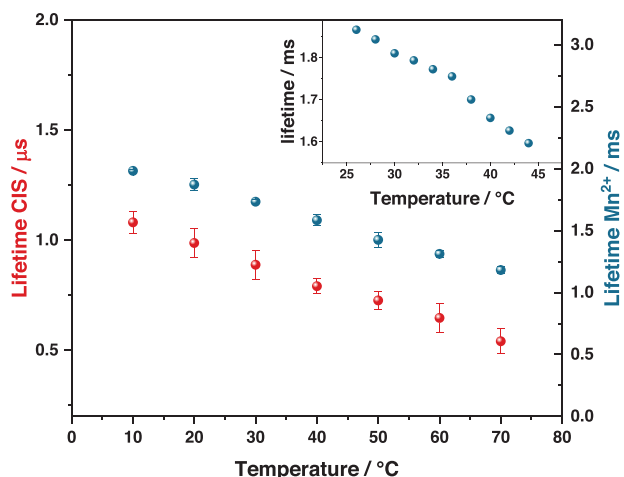
5. Conclusions

Manganese doped CIZS-QDs (Mn-CIZSγ) were synthesized as colloidally stable dispersion in water by a low-temperature hydrothermal synthesis. The synthesis has proven to be tolerant to In:Cu ratio as high as 37, and it enabled the incorporation of Mn^{2+} within the CIZS crystal structure. All manganese doped quantum dots showed both the emission related to CIZS (μs-timescale) and the long-lived emission (approximately ms) around 620 nm ascribed to Mn^{2+} centers. Furthermore, the relative contribution of Mn^{2+} emissions to the overall emission is strongly dependent on the In:Cu ratio, increasing upon decreasing copper content. Mn^{2+} emission is sensitized with a threshold energy of excitation (2.5 eV), higher than the energy of the emissive state (2 eV), suggesting a complex sensitization mechanism.

Given the low toxicity of the investigated materials and the water solubility of all samples, the emission of Mn-CIZSγ samples was monitored in the temperature range 10–80 °C to test them as luminescent thermometry probes. The emission of both CIZS and Mn^{2+} has decreasing lifetime upon increasing

Figure 7. Temperature dependence of the photoluminescence lifetime of Mn-CIZS11 in bidistilled water (main graph) and PBS (inset). Red and blue dots refer to CIZS and Mn^{2+} emission, respectively. All emission decays are recorded with $\lambda_{exc} = 375$ nm and $\lambda_{em} = 620$ nm.

**ADVANCED
SCIENCE NEWS**

www.advancedsciencenews.com

**NANO · MICRO
small**

www.small-journal.com

temperature, and in particular the Mn^{2+} emission has slope 15 µs K^{-1} when tested in phosphate buffer in the range 25–45 °C, mimicking physiological conditions. In addition to that, all photophysical properties of the samples proved to be reversible within the temperature range analyzed and independent on other possible biological stimuli such as oxygen concentration, interfering anions and pH variations.

In summary, the presented results demonstrate that the prepared quantum dots are ideal platforms for the development of easy-to-produce, cost-effective bioimaging temperature sensors with a quantitative time-gated detection, which eliminates scattered excitation light and autofluorescence of the sample. These properties are coupled to the insensitivity to dioxygen quenching, which enables temperature measurements in differently oxygenated samples.

6. Experimental Section

Materials and Methods: $CuCl_2$ (98%), $InCl_3$ (99%), $MnSO_4 \cdot H_2O$ (97%), $Zn(AcO)_2$ (99%), Na_2S (≥90%), NaOH (98%), HNO_3 (65%). HCl (37%), *L*-glutathione reduced (*L*-GSH, 99%), sodium citrate (99%), and thiourea (99%) were purchased from Sigma-Aldrich and used with no additional purification. Water was deionized by reverse osmometry with an Elga Purelab Classic purification system (13 MΩ cm). Acetone (ACS) was purchased by Sigma-Aldrich and used with no further purification.

Synthesis of Mn-CIZSγ[18]: The synthesis of the quantum dots was performed in closed vessels heated with a heating plate equipped with a thermocouple to control the temperature. The following stock solutions were prepared: $CuCl_2$ 0.013 M in water, $InCl_3$ 0.25 M in ethanol, $Na_3C_6H_5O_7$ 0.4 M in water, $MnSO_4$ 0.01 M in water, Na_2S 1 M in water and, for the second step of the synthesis (see Figure 1), a solution containing $Zn(OAc)_2$ 0.04 M, $SC(NH_2)_2$ 0.03 M, GSH 0.06 M in water. In a typical synthesis, a variable volume of $CuCl_2$ stock solution was added to 10 mL of deionized water, together with 80 µL (20 µmol) of $InCl_3$ stock solution and variable volumes of $MnSO_4$ stock solution to obtain the desired In:Cu and Mn:In feeding ratios (Table S1, Supporting Information). Subsequently, 200 µL of citrate stock solution (80 µmol) was added to the solution, which turned to light blue due to the Cu(II)-citrate complex formation. L-glutathione (18 mg, 60 µmol) was then added to the reaction vessel. After that, 96 µL (96 µmol) of Na_2S stock solution was added to the solution and the reaction vessel was stirred in a pre-heated bath at 95 °C for 40 min for the core growth. The addition of Na_2S causes an instantaneous color change, indicating that the reaction started as soon as the sulfur source was added to the reaction. At the end of the 40 min, 3 mL of the Zn stock solution was added to the reaction vessel. The mixture was stirred at 95 °C for 45 additional minutes. The reaction was stopped upon cooling the reaction vessel with a cold-water bath. The as-synthesized quantum dots were precipitated in acetone (25 mL) and then redispersed in 5 mL of bidistilled water or phosphate buffer (PBS, pH = 7.4) and stored at room temperature. In these conditions, they proved to be stable upon several months.

Synthesis of IZS: 80 µL of indium stock solution, 200 µL of citrate stock solution and 18 mg of *L*-GSH were mixed with 10 mL of water in a closed vessel. Subsequently, 96 µL of Na_2S stock solution was added to the reaction pot and the mixture is kept stirring at 95 °C for 40 min. After that, 3 mL of the Zn stock solution was added to the reaction vessel and the mixture was stirred at 95 °C for 45 additional minutes. The reaction was stopped upon cooling the reaction vessel in a cold water bath and the sample was precipitated in acetone and re-dispersed in 5 mL of bidistilled water.

Material Characterization: Elemental composition of CIZS QDs was determined via an Agilent 4210 MP-AES atomic emission spectrometer. To this purpose, around 10 drops of HCl 1 M was added to 1 mL of the acetone-purified Mn-CIZSγ. This led to complete precipitation of the quantum dots, which could be centrifuged (5 min, 8000 rpm) to obtain a clean supernatant and a colored powder. The powder was then digested into 3 mL of 7 M nitric acid.

Powder XRD measurements were performed on a Panalytical X'Pert Pro powder diffractometer equipped with a Cu X-ray tube (Kα radiation, 1.54184 Å, 40 mA, 40 kV), with a Bragg-Brentano configuration and X'celerator detector. Typically, a suspension of Mn-CIZSγ in water was precipitated in acetone, dried at rotary evaporator and rotative pump, and deposited onto a zero-background silicon sample holder. A continuous scan from 15° to 70° was performed with an acquisition time of 15 min.

A FEI Tecnai F20 high-resolution transmission electron microscope (HRTEM), equipped with a Schottky transmitter operating at 200 kV was used for the estimation of details on crystal structure and nanoscale morphology. High angle annular dark field (HAADF)-STEM micrographs were recorded to improve the dimensional analysis of the nanocrystals. The elemental analysis was carried out by energy dispersive X-ray spectroscopy (EDS), coupled with STEM-HAADF to map the elemental distribution.

Photophysical Characterization: Photophysical measurements were carried out in air-equilibrated bidistilled water at 298 K, unless otherwise noted. UV−visible absorption spectra were recorded with a Perkin Elmer λ650 spectrophotometer, using quartz cells with a 1.0 cm path length. The bandgap of Mn-CIZSγ was determined through the second derivative method.[57] Emission and excitation spectra were obtained with a Perkin Elmer LS-50 spectrofluorometer equipped with a Hamamatsu R928 phototube. CIZS emission was monitored in the time interval 0–0.02 ms (short gate), whereas Mn^{2+} emission was recorded in the time interval 0.2–5 ms (long gate). The overall emission of Mn-CIZSγ samples was monitored in the time gate 0–5 ms (full gate). In the short gate measurement less than 2% of the total Mn emission is detected as estimated on the basis of its lifetime, whereas in the long-gate acquisition CIZS emission has completely decayed, which allowed to consider them fully resolved in time. The relative contribution of Mn^{2+} and CIZS emission to the overall emission of Mn-CIZSγ samples was calculated by combining short-gate and long-gate measurements with different percentage coefficients until the sum spectrum corresponds to the full-gate spectrum of the Mn-CIZSγ sample under analysis. Emission quantum yields were measured following the method of Crosby and Demas[58] (standard used: $[Ru(bpy)_3]^{2+}$ in air-equilibrated aqueous solution $\Phi = 0.0407$).[59] PL lifetime measurements of solutions of Mn-CIZSγ in the range 0.5 ns to 10 µs were performed by an Edinburgh FLS920 spectrofluorometer equipped with a TCC900 card for data acquisition in time-correlated single photon counting experiments (0.2 ns time resolution) with an LDH-P-C-405 pulsed diode laser. PL lifetime measurements of solutions of Mn-CIZSγ in the range 1 to 10 ms were performed by an Edinburgh FLS1000 spectrofluorometer equipped with a microsecond flash lamp.

Temperature Sensing: For temperature-controlled experiments, the temperature of the cuvette was controlled via a Julabo F12 temperature controller unit directly connected to the spectrofluorometer cuvette holder. The measurements were repeated 4 times, and the values reported are the mean value together with the calculated absolute error values.

The estimated experimental errors are: 2 nm on the band maxima, 5% on the luminescence lifetime, 10% on the emission quantum yield.

Supporting Information

Supporting Information is available from the Wiley Online Library or from the author.

Acknowledgements

Conflict of Interest

The authors declare no conflict of interest.

Data Availability Statement

The data that support the findings of this study are available from the corresponding author upon reasonable request.

Keywords

[1] S. Kargozar, S. J. Hoseini, P. B. Milan, S. Hooshmand, H. Kim, M. Mozafari, *Biotechnol. J.* **2020**, *15*, 2000117.

[2] T. Jamieson, R. Bakhshi, D. Petrova, R. Pocock, M. Imani, A. M. Seifalian, *Biomaterials* **2007**, *28*, 4717.

[3] S. Chinnathambi, S. Chen, S. Ganesan, N. Hanagata, *Adv. Healthcare Mater.* **2014**, *3*, 10.

[4] Z. Wu, Y. Ou, M. Cai, Y. Wang, R. Tang, Y. Xia, *Adv. Opt. Mater.* **2023**, *11*, 2201577.

[5] G. Morselli, M. Villa, A. Fermi, K. Critchley, P. Ceroni, *Nanoscale Horiz.* **2021**, *6*, 676.

[6] C. Lin, X. Song, W. Ye, T. Liu, M. Rong, L. Niu, *J. Anal. Test.* **2024**, *8*, 95.

[7] B. Harrington, Z. Ye, L. Signor, A. D. Pickel, *ACS Nanosci. Au* **2024**, *4*, 30.

[8] C. D. S. Brites, R. Marin, M. Suta, A. N. Carneiro Neto, E. Ximendes, D. Jaque, L. D. Carlos, *Adv. Mater.* **2023**, *35*, 2302749.

[9] H. Zhao, A. Vomiero, F. Rosei, *Small* **2020**, *16*, 2000804.

[10] X. Long, X. Tan, Y. He, G. Zou, *J. Mater. Chem. C* **2017**, *5*, 12393.

[11] T. Chen, L. Li, X. Lin, Z. Yang, W. Zou, Y. Chen, J. Xu, D. Liu, X. Wang, G. Lin, *Nanotoxicology* **2020**, *14*, 372.

[12] C. Arriaza-Echanes, J. L. Campo-Giraldo, C. P. Quezada, R. Espinoza-González, P. Rivas-Álvarez, M. Pacheco, D. Bravo, J. M. Pérez-Donoso, *Arabian J. Chem.* **2021**, *14*, 103176.

[13] R. Marin, A. Vivian, A. Skripka, A. Migliori, V. Morandi, F. Enrichi, F. Vetrone, P. Ceroni, C. Aprile, P. Canton, *ACS Appl. Nano Mater.* **2019**, *2*, 2426.

[14] a) Z. Ziani, C. Bellatreccia, F. P. Battaglia, G. Morselli, A. Gradone, P. Ceroni, M. Villa, *Nanoscale* **2024**, *16*, 12947; b) G. Morselli, C. Bellatreccia, M. Mazzanti, V. Cristino, A. Ianniello, S. Caramori, R. Mazzaro, P. Ceroni, *Adv. Opt. Mat.* **2024**, 2400259.

[15] H. Zhong, Z. Bai, B. Zou, *J. Phys. Chem. Lett.* **2012**, *3*, 3167.

[16] N. Tsolekile, S. Nahle, N. Zikalala, S. Parani, E. H. M. Sakho, O. Joubert, M. C. Matoetoe, S. P. Songca, O. S. Oluwafemi, *Sci. Rep.* **2020**, *10*, 4936.

[17] D. H. Jara, K. G. Stamplecoskie, P. V. Kamat, *J. Phys. Chem. Lett.* **2016**, *7*, 1452.

[18] Y. Chen, S. Li, L. Huang, D. Pan, *Inorg. Chem.* **2013**, *52*, 7819.

[19] X. Yuan, R. Ma, W. Zhang, J. Hua, X. Meng, X. Zhong, J. Zhang, J. Zhao, H. Li, *ACS Appl. Mater. Interfaces* **2015**, *7*, 8659.

[20] L. Peng, D. Li, Z. Zhang, K. Huang, Y. Zhang, Z. Shi, R. Xie, W. Yang, *Nano Res.* **2015**, *8*, 3316.

[21] B. Huang, Q. Dai, N. Zhuo, Q. Jiang, F. Shi, H. Wang, H. Zhang, C. Liao, Y. Cui, J. Zhang, *J. Appl. Phys.* **2014**, *116*, 094303.

[22] S. Ghosh, M. Saha, V. D. Ashok, A. Chatterjee, S. K. De, *Nanotechnology* **2016**, *27*, 155708.

[23] S. Cao, C. Li, L. Wang, M. Shang, G. Wei, J. Zheng, W. Yang, *Sci. Rep.* **2014**, *4*, 7510.

[24] M. A. Abate, K. Dehvari, J.-Y. Chang, K. Waki, *Dalton Trans* **2019**, *48*, 16115.

[25] R. Wang, X. Tong, A. Imran Channa, Q. Zeng, J. Sun, C. Liu, X. Li, J. Xu, F. Lin, G. Singh Selopal, F. Rosei, Y. Zhang, J. Wu, H. Zhao, A. Vomiero, X. Sun, Z. M. Wang, *J. Mater. Chem. A* **2020**, *8*, 10736.

[26] V. Balzani, *Curr. Opin. Chem. Biol.* **2003**, *7*, 657.

[27] F. Romano, Y. Yu, B. A. Korgel, G. Bergamini, P. Ceroni, *Top. Curr. Chem.* **2016**, *374*, 53.

[28] F. Romano, S. Angeloni, G. Morselli, R. Mazzaro, V. Morandi, J. R. Shell, X. Cao, B. W. Pogue, P. Ceroni, *Nanoscale* **2020**, *12*, 7921.

[29] K. Y. Zhang, Q. Yu, H. Wei, S. Liu, Q. Zhao, W. Huang, *Chem. Rev.* **2018**, *118*, 1770.

[30] Q. A. Akkerman, A. Genovese, C. George, M. Prato, I. Moreels, A. Casu, S. Marras, A. Curcio, A. Scarpellini, T. Pellegrino, L. Manna, V. Lesnyak, *ACS Nano* **2015**, *9*, 521.

[31] L. De Trizio, M. Prato, A. Genovese, A. Casu, M. Povia, R. Simonutti, M. J. P. Alcocer, C. D'Andrea, F. Tassone, L. Manna, *Chem. Mater.* **2012**, *24*, 2400.

[32] G. Manna, S. Jana, R. Bose, N. Pradhan, *J. Phys. Chem. Lett.* **2012**, *3*, 2528.

[33] M. Jiao, Y. Li, Y. Jia, Z. Yang, X. Luo, *Sens. Actuators, B* **2019**, *294*, 32.

[34] Y. Xu, T. Chen, X. Hu, W. Jiang, L. Wang, W. Jiang, J. Liu, *J. Colloid Interface Sci.* **2017**, *496*, 479.

[35] N. Eliasson, B. P. Rimgard, A. Castner, C.-W. Tai, S. Ott, H. Tian, L. Hammarström, *J. Phys. Chem. C* **2021**, *125*, 14751.

[36] J. Hua, Y. Du, Q. Wei, X. Yuan, J. Wang, J. Zhao, H. Li, *Phys. B Condens. Matter* **2016**, *491*, 46.

[37] P. Ilaiyaraja, P. S. V. Mocherla, T. K. Srinivasan, C. Sudakar, *ACS Appl. Mater. Interfaces* **2016**, *8*, 12456.

[38] G. Zaiats, S. Kinge, P. V. Kamat, *J. Phys. Chem. C* **2016**, *120*, 10641.

[39] T. Debnath, H. N. Ghosh, *J. Phys. Chem. Lett.* **2019**, *10*, 6227.

[40] A. J. Van Bunningen, S. T. Keizer, A. Meijerink, *J. Mater. Chem. C* **2023**, *11*, 8961.

[41] C. Harrison, B. Gallian, G. Dong, Y. Wang, J. Zhao, X. Zhu, *J. Nanopart. Res.* **2019**, *21*, 248.

[42] L. Peng, K. Huang, Z. Zhang, Y. Zhang, Z. Shi, R. Xie, W. Yang, *ChemPhysChem* **2016**, *17*, 752.

[43] Y. Liu, M. L. Zaffalon, J. Zito, F. Cova, F. Moro, M. Fanciulli, D. Zhu, S. Toso, Z. Xia, I. Infante, L. De Trizio, S. Brovelli, L. Manna, *Chem. Mater.* **2022**, *34*, 8603.

[44] H. Bahmani Jalali, A. Pianetti, J. Zito, M. Imran, M. Campolucci, Y. P. Ivanov, F. Locardi, I. Infante, G. Divitini, S. Brovelli, L. Manna, F. Di Stasio, *ACS Energy Lett.* **2022**, *7*, 1850.

[45] P. K. R., R. Viswanatha, *APL Mater.* **2020**, *8*, 020901.

[46] P. Mondal, S. Sathiyamani, K. Gahlot, R. Viswanatha, *J. Phys. Chem. C* **2021**, *125*, 11007.

[47] K. Gahlot, K. R. Pradeep, A. Camellini, G. Sirigu, G. Cerullo, M. Zavelani-Rossi, A. Singh, U. V. Waghmare, R. Viswanatha, *ACS Energy Lett.* **2019**, *4*, 729.

[48] S. V. Eliseeva, J.-C. G. Bünzli, *Chem. Soc. Rev.* **2010**, *39*, 189.

[49] M. D. Ward, *Coord. Chem. Rev.* **2010**, *254*, 2634.

[50] P. Kumbhakar, A. R. Karmakar, G. P. Das, J. Chakraborty, C. S. Tiwary, P. Kumbhakar, *Nanoscale* **2021**, *13*, 2946.

[51] P. Yu, X. Wen, Y.-R. Toh, J. Tang, *J. Phys. Chem. C* **2012**, *116*, 25552.

[52] S. Kalytchuk, K. Poláková, Y. Wang, J. P. Froning, K. Cepe, A. L. Rogach, R. Zbořil, *ACS Nano* **2017**, *11*, 1432.

[53] N. Ük, S. Aykut, H. Jahangiri, I. Nar, C. Ünlü, *New J. Chem.* **2024**, *48*, 10074.

[54] G. Huang, C. Wang, X. Xu, Y. Cui, *RSC Adv.* **2016**, *6*, 58113.

[55] S. Cao, J. Zheng, J. Zhao, Z. Yang, M. Shang, C. Li, W. Yang, X. Fang, *Adv. Funct. Mater.* **2016**, *26*, 7224.

[56] O. Stroyuk, A. Raevskaya, F. Spranger, N. Gaponik, D. R. T. Zahn, *ChemPhysChem* **2019**, *20*, 1640.

[57] M. Booth, A. P. Brown, S. D. Evans, K. Critchley, *Chem. Mater.* **2012**, *24*, 2064.

[58] G. A. Crosby, J. N. Demas, *J. Phys. Chem.* **1971**, *75*, 991.

[59] K. Suzuki, A. Kobayashi, S. Kaneko, K. Takehira, T. Yoshihara, H. Ishida, Y. Shiina, S. Oishi, S. Tobita, *Phys. Chem. Chem. Phys.* **2009**, *11*, 9850.